THE UNIVERSITY of EDINBURGH

Edinburgh Research Explorer

Characteristics of sprays produced by coaxial non-swirling and swirling air-water jets with high aerodynamic Weber numbers

Citation for published version:
Liang, Y, Johansen, L & Linne, M 2022, 'Characteristics of sprays produced by coaxial non-swirling and swirling air-water jets with high aerodynamic Weber numbers', *Physics of Fluids*, vol. 34, no. 10, 103604. https://doi.org/10.1063/5.0107480

Digital Object Identifier (DOI):
10.1063/5.0107480

Link:
Link to publication record in Edinburgh Research Explorer

Document Version:
Peer reviewed version

Published In:
Physics of Fluids

General rights
Copyright for the publications made accessible via the Edinburgh Research Explorer is retained by the author(s) and / or other copyright owners and it is a condition of accessing these publications that users recognise and abide by the legal requirements associated with these rights.

Take down policy
The University of Edinburgh has made every reasonable effort to ensure that Edinburgh Research Explorer content complies with UK legislation. If you believe that the public display of this file breaches copyright please contact openaccess@ed.ac.uk providing details, and we will remove access to the work immediately and investigate your claim.

OPEN ACCESS

Download date: 27. Oct. 2022

Characteristics of sprays produced by coaxial non-swirling and swirling air-water jets with high aerodynamic Weber numbers

Yifan Liang (梁依帆),[1] Lars Christian Johansen,[1] and Mark Linne[1]
Institute for Multiscale Thermofluids, School of Engineering, University of Edinburgh, James Clerk Maxwell Building,
Peter Guthrie Tait Road, Edinburgh, EH9 3FD, United Kingdom

(*Electronic mail: yifan.liang@ed.ac.uk)

(Dated: 10 September 2022)

This paper describes part of an experimental study on shear-based spray formation. A laminar liquid jet was ejected inside co-annular non-swirling and swirling air streams. The aerodynamic Weber numbers (We_A) and swirl numbers (S) of the flow cases ranged from 256 to 1426 and from 0 to 3.9, respectively. The aim of this paper is to investigate how S and We_A influence the breakup of a central laminar liquid jet within the fiber-type atomization regime. High-speed shadowgraphy was utilised to visualise the spray behaviour, while Phase Doppler Interferometry (PDI) was utilised to measure the droplet size and velocity distributions. It was found that as S increases, atomization is improved in a way that the droplets are blown outward from the central axis of the nozzle. However, for some specific flow cases, the median droplet diameter (D) does not appear to be related to S. Those specific flow cases are discussed in this work. For $S \geq 0.3$, upward motion of droplets located at the central axis of the nozzle was observed, which was caused by recirculating air flows. In addition, it was found that when S increases to 2.5, recirculating air flows start to penetrate to the water exit, which momentarily stops portions of the central laminar water jets from exiting. This pattern will be called turn-off behaviour in this report. In order to study the underlying mechanisms behind the turn-off behaviour, proper orthogonal decomposition (POD) was performed on the shadowgrams. It was found that the timing of turn-off initiation is random.

I. INTRODUCTION

Sprays are critical for many industrial applications and yet there are no fully predictive models for spray formation, owing in part to an absence of detailed spray formation statistics. Lefebvre and McDonell[1] pointed out that there are three main breakup mechanisms which influence spray performance, namely, turbulence in the liquid, aerodynamic forces acting on the gas-liquid interface (also called "shear forces"), and cavitation inside the nozzle. Hence, in order to set up a database for spray formation, these three breakup mechanisms should be separated from one another. Otherwise, computational fluid dynamics (CFD) validation will become more complicated and uncertain because spray formation might simultaneously result from interaction of those three breakup mechanisms. The aim of the program described in this paper (and in a companion paper published earlier by Liang, Johansen, and Linne[2]) is to develop a comprehensive database for spray formation caused by shear forces alone. In both cases, the liquid jet was laminar. It is our view that the use of a laminar liquid jet simplifies model validation.

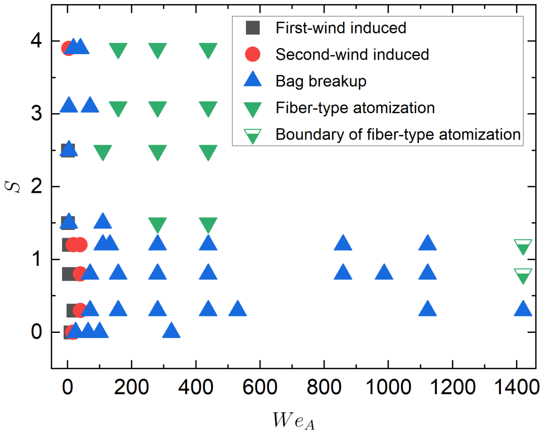

FIG. 1. Regime map characterised by S and We_A. Note that the first-wind induced, second-wind induced and bag breakup regimes were investigated in an earlier, companion paper (reproduced from Liang, Johansen, and Linne[2], with the permission of AIP Publishing). The fiber-type atomization regime is investigated and discussed in this paper.

In our earlier, companion paper, Liang, Johansen, and Linne[2] performed a morphological study over a wide range of operating conditions and established a regime map characterised by the swirl number S (defined in Equation 5 below) and the aerodynamic Weber number We_A (defined in Equation 2 below). A database containing the spray morphology information from the earlier paper is available to interested parties[3]. In that work, four types of breakup regimes were identified (first-wind induced, second-wind induced, bag breakup and fiber-type atomization), as shown in Figure 1. In the first paper, Liang, Johansen, and Linne[2] investigated spray formation caused by shear forces acting on a laminar liquid jet within the first-wind induced, second-wind induced and bag breakup regimes (the first three regimes in Figure 1). They reported and analyzed liquid breakup lengths, axial location of first droplet formation, large-scale, shear instabilities (all via high-speed shadowgraphy and image analysis) and air flow fields (via Stereo Particle Image Velocimetry, SPIV) for those three breakup regimes. In that work, both S and We_A determine the type of breakup regime for a laminar liquid jet in a coaxial swirling air flow. For those three breakup regimes, however, We_A is much smaller than what is required for fiber-type atomization.

This paper focuses on spray formation within the fiber-type atomization regime or on the boundary of fiber-type atomization regime, where We_A is much higher than the flow cases investigated in the companion paper. Few droplets were observed when investigating the first three breakup regimes, and the drop sizes were large when compared with the flow cases reported in this paper. Here the flow-field shortened and many smaller drops were observed. Because the high We_A flow-fields were so different from the three flow-fields in the less highly atomizing regimes, it was necessary to apply a different set of measurements and a different approach to analysis in the work reported here.

A complete, detailed, shear-based spray formation database should include the quantities measured in the earlier paper, together with the results reported here. In the work reported here, we investigated how S and We_A influence the breakup of a central laminar liquid jet under fiber-type atomization. Phase Doppler Interferometry (PDI) was utilized to measure the droplet size and velocity distributions (PDI was not used in the earlier work). The Stereo Particle Image Velocimetry (SPIV) results reported by Liang, Johansen, and Linne[2] have some relevance to the high We_A flows and they will be discussed here as well. In addition, we observed a turn-off behaviour for two flow cases with high We_A, and it was analyzed using proper orthogonal decomposition (POD) in this paper (this behaviour is discussed in more detail in Sec. III B). A database containing the spray morphology and droplet size and velocity distributions reported in this paper has been prepared and it is available to interested parties[4].

In order to study the spray performance of a coaxial non-swirling gas-liquid jet, Varga, Lasheras, and Hopfinger[5] ejected a water or ethanol jet into coflowing air without swirl. The Reynolds numbers for the water jet ranged from 543 to 16567, and the aerodynamic Weber numbers ranged from 6 to 437. They utilised Phase Doppler Interferometry (PDI) to obtain the droplet size distributions, and developed a phenomenological breakup model to predict the Rayleigh-Taylor wavelengths and primary mean droplet sizes, both of which provided good agreement with their experimental data. Yang *et al.*[6] started from a stability analysis on the coaxial non-swirling air-liquid jet, and proposed a theoretical correlation to predict the Sauter mean diameter (D_{32}). The working fluids they used for the central liquid jet were water and ethanol, and their Reynolds numbers for the water jet ranged from 1597 to 5301. Their correlation for D_{32} collapsed well onto the experimental data given by Varga, Lasheras, and Hopfinger[5]. Lasheras, Villermaux, and Hopfinger[7] used high-speed shadowgraphy and PDI to investigate a coaxial non-swirling air-water jet. The liquid Reynolds numbers ranged from 569 to 5689. For near-field breakup and atomization, they proposed an entrainment model to describe qualitatively the dependence of the measured liquid shedding frequency on the gas to liquid momentum flux ratio (M). For far-field breakup and atomization, they proposed two atomization models to explain the dependence of the breakup and coalesence of the droplets on the local turbulent dissipation rate in the gas stream, respectively. They found that secondary breakup and coalescence of the droplets in the far field of the spray jet are mainly influenced by the total kinetic energy flux (mainly contained in the air jet) per unit total mass of air and water. Hardalupas and Whitelaw[8] investigated a coaxial non-swirling air-water jet over a wide range of liquid Reynolds numbers, $Re_l(10^4 - 5.5\times10^4)$, and aerodynamic Weber numbers, $We_A(200-3500)$. They utilised PDI to measure the D_{32} distributions, and studied the effects of the liquid tube diameter, converging gaseous jet exit and liquid tube recess on the D_{32} distributions. Eroglu and Chigier[9] ejected a water jet into coflowing air without swirl, and measured the initial drop size and velocity distributions using PDI. Their liquid Reynolds numbers ranged from 1097 to 4379. They found that D_{32} grows when liquid supply pressure increases or air supply pressure diminishes. They also found that the droplet mean velocities reach their minimum at the central axis of the nozzle, and the maximum droplet mean velocities appear on the periphery of the spray.

In order to investigate how air swirl influences spray performance, Hopfinger and Lasheras[10] investigated the breakup of a water jet by a coaxial swirling air jet over a wide range of liquid Reynolds numbers, $Re_l(740-11400)$, and gas to liquid momentum flux ratios, $M(1-1000)$. They found that when the swirl number (S) goes beyond a critical swirl number (S_{cr}), hollow-cone spray structures caused by the central recirculation of the swirling air flows were observed. The hollow-cone spray structures were also observed by Machicoane *et al.*[11] when they used high-speed X-ray radiography to investigate a central water jet surrounded by a coaxial air jet with and without swirl over a wide range of $Re_l(1100-6500)$, $M(6-202)$ and $S(0-1)$. Hardalupas and Whitelaw[12] investigated the breakup of a turbulent water jet by a co-annular air stream with S in the range of $\sim 0-7.9$. They used PDI to measure the diameters, velocities and liquid fluxes of the droplets over a wide range of aerodynamic Weber numbers, $We_A(230-630)$. They observed hollow cone-spray structures caused by the central recirculation of the swirling air flows with high S, which was consistent with what Hopfinger and Lasheras[10] found. Hardalupas and Whitelaw[12] found that the droplet size is related to the local Weber number (We_D) of the droplet (here $We_D = \rho_g(u_g-u_l)^2 d/\sigma_l$, where ρ_g is the density of the gas, u_g is the local velocity of the gas phase, u_l is the local velocity of the droplet, d is the droplet diameter, and σ_l is the surface tension of the liquid). They also found that when $S > 0.3$, atomization is improved because droplets are blown outward away from the central axis of the nozzle. However, for the breakup of a central laminar liquid jet by a coaxial swirling air stream, the droplet size and velocity distributions remain unknown and are explored in this paper.

Lasheras and Hopfinger[13] measured the droplet size distributions for the breakup of a central liquid jet surrounded by a coaxial swirling air stream with S in the range of $0-0.4$, and pointed out that when S goes beyond S_{cr}, the spray can be divided into three regions in terms of D_{32}: an external region where D_{32} reaches its maximum; an internal region where the central recirculating air flow happens and D_{32} reaches its minimum; and a middle hollow conical region where the D_{32} distribution is bimodal. They also found that this middle hollow conical region is pushed outward with the increase of S, and that the sizes of the droplets located in that region are independent of S, while the sizes of the droplets located in the inner region depend on S. Lasheras and Hopfinger[13] pointed out that the mechanism of the atomization of the droplets in the outer region is primary breakup. However, for the breakup of a central laminar liquid jet by a coaxial swirling air stream with S in the range of $\sim 0.4-3.9$, the droplet size and velocity distributions remain unknown and are explored in this paper.

Dunand, Carreau, and Roger[14] used PDI, tomography and an optical fiber probe to investigate the breakup of a turbulent water jet by a coaxial air jet with S and M in the ranges of $\sim 0-0.6$ and $\sim 3-13.3$, respectively. They found that when S goes beyond S_{cr}, large droplets with ballistic trajectories appear on the jet periphery, while small droplets are located in the hollow-cone region caused by the recirculating air flows. They also found that when $S < S_{\mathrm{cr}}$, big droplets are located near the central axis of the nozzle, while small droplets appear on the outer edge of the jet. However, their central liquid jet is turbulent, which means that the atomization is simultaneously caused by two breakup mechanisms (turbulence in the liquid and shear forces). In order to develop a comprehensive validation database for research groups in CFD, those two breakup mechanisms should be isolated from each other. In this work, droplet size and velocity measurements were performed for spray formation caused by shear forces, in part by removing turbulence from the liquid jet.

In order to understand how the strength of the air swirl affects the instability of the central water jet, some stability analyses have been performed on the coaxial liquid jet surrounded by a swirling gas stream[15–17]. However, for the breakup of a coaxial liquid jet in a swirling gas stream, a drop size model has not been developed, and a droplet size database that can be used to provide validation on a drop size model needs to be established. Although research on the droplet sizes of coaxial non-swirling jets has been done[5–9], only a handful of studies on the droplet sizes of coaxial swirling jets have been reported. Hardalupas and Whitelaw[12] measured the droplet size and velocity distributions for the breakup of a turbulent water jet by a co-annular air stream with S in the range of $\sim 0-7.9$. However, the droplet size and velocity distributions for the breakup of a central laminar water jet by a swirling air stream with S in the range of $\sim 0-7.9$ remain unknown. Although Lasheras and Hopfinger[13] investigated the droplet size distributions for a coaxial swirling air-liquid jet with S in the range of $\sim 0-0.4$, the droplet size and velocity distributions for the breakup of a central laminar water jet by a swirling air stream with S in the range of $\sim 0.4-3.9$ remain unknown and are explored in this paper.

The paper is organized as follows. Section II describes the experimental setup and procedure. Section III presents the annular air flow fields obtained from the companion paper[2], droplet size and velocity distributions, and POD analysis on the turn-off behaviours. Section IV develops conclusions for this part of the program work.

TABLE I. Vane angles for all the air swirlers.

S[a]	θ[b]
0.3	21.1°
0.8	45.8°
1.2	57.1°
1.5	62.6°
2.5	72.7°
3.1	75.9°
3.9	78.7°

[a] Swirl number
[b] Vane angle

II. EXPERIMENTAL SETUP AND PROCEDURE

A. Overall Setup

In this paper we report experimental results based on the same experimental facility described by Liang, Johansen, and Linne[2]. That paper described the experimental apparatus in full detail. Here we present a shorter introduction to the system. The central liquid jet and annular gas stream are water and air, respectively. Two mass flow controllers (MFC) (Bronkhorst Inc) are used to control and measure the air and water flow rates. The nozzle is the same as the one investigated by Liang, Johansen, and Linne[2] (see Fig. 2). The inner diameters of the liquid and co-flow tubes are 4 mm and 10 mm, respectively. The outer diameters of the liquid and co-flow tubes are 5 mm and 14 mm, respectively. In order to introduce swirl into the air, a swirler is added to the inner surface of the co-flow tube. There are eight types of air swirlers with different vane angles. A vane angle is defined as the angle between a tangent at the tip of the vane and a vertical line. The magnitudes of the vane angles for those air swirlers are shown in Table I. All the air swirlers have four-star shapes. The cross-sectional areas of the air outlets with and without the air swirler are 28.09 mm^2 and 58.9 mm^2, respectively. The lengths of the water tubes and co-flow tubes are 140 mm and 43 mm, respectively. The Reynolds number of the central water jet is kept at 480 for all the flow cases to ensure that the laminar pipe flow becomes fully developed before it leaves the nozzle exit. According to White[18], Schlichting and Gersten[19] and White[20], the entrance length (L_e) for a laminar pipe flow is given by:

$$L_e = 0.06 \times Re_{D_I} \times D_I, \tag{1}$$

Where, D_I is the inner diameter of the pipe, and Re_{D_I} is the Reynolds number based on D_I. The L_e for the laminar water flow in this work is given by:

$$L_e = 105.12 \text{ mm} < 140 \text{ mm (length of the water tube)},$$

which means that the central laminar water flow becomes fully developed before it leaves the nozzle exit. This conclusion was confirmed by high-speed shadowgrams of the jet in the absence of any air flow.

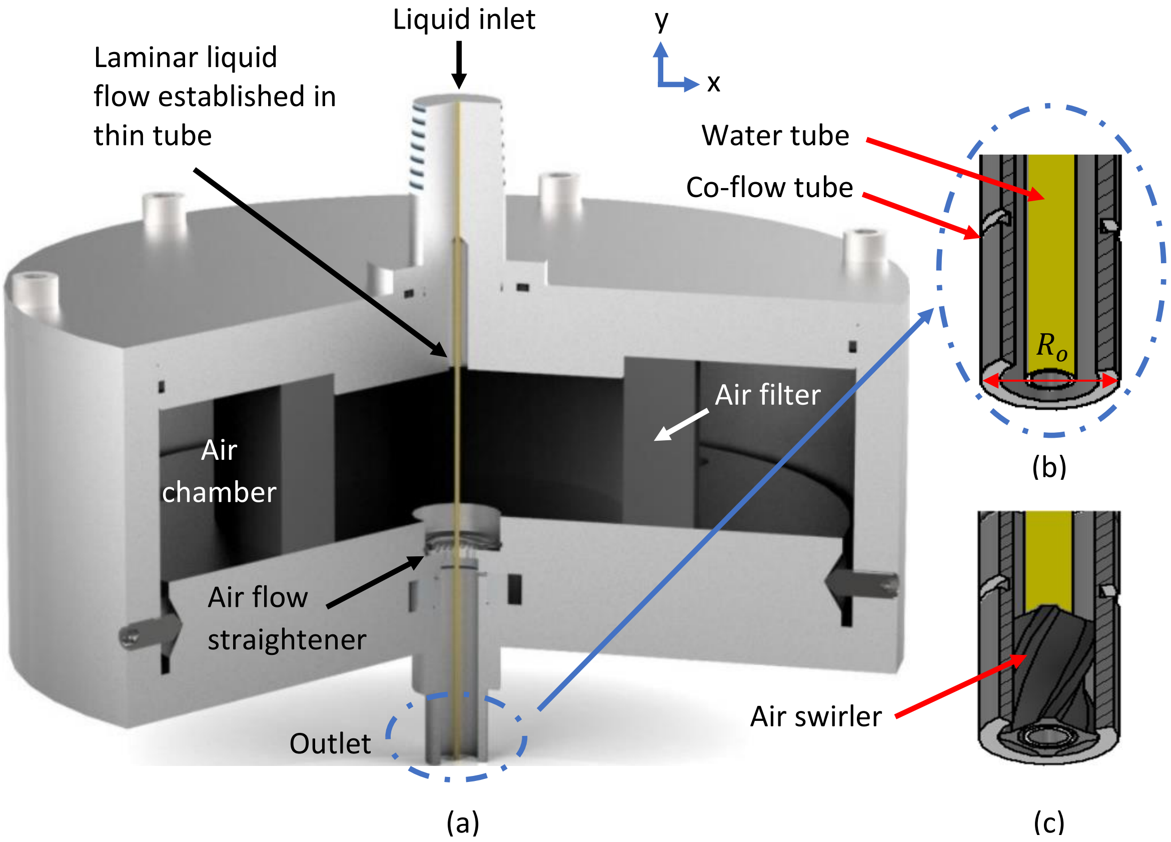

FIG. 2. Images of the atomizer. (a) Broken-out view of the atomizer. (b) Broken-out view of the co-flow tube without air swirler attached on it. (c) Broken-out view of the co-flow tube with the air swirler (reproduced from Liang, Johansen, and Linne[2], with the permission of AIP Publishing).

B. Operating Conditions for the Atomizer

The characteristics of twin-fluid atomization are related to the fluid material properties and the relative velocities between those two fluids. In this work, three non-dimensional parameters were used to describe the operating conditions of the twin-fluid atomizer. They are aerodynamic Weber number (We_A), the liquid Reynolds number (Re_l), and the gas to liquid momentum flux ratio (M), given by:

$$We_A = \frac{\rho_g \left(U_g - U_l\right)^2 D_l}{\sigma_l}, \tag{2}$$

$$Re_l = \frac{U_l D_l}{\nu_l}, \tag{3}$$

$$M = \frac{\rho_g U_g^2}{\rho_l U_l^2}. \tag{4}$$

Here, ρ_l is the density of the liquid, ρ_g is the density of the gas , U_g is the gas velocity, U_l is the liquid velocity, D_l is the diameter of the liquid tube, D_g is the diameter of the co-flow tube, σ_l is the surface tension of the liquid, ν_l is the kinematic viscosity of the liquid, ν_g is the kinematic viscosity of the gas. U_l and U_g are the axial bulk velocities of the liquid jet and gas stream at the nozzle exit, respectively. Additionally, the swirl number (S), which is the ratio of the axial flux of swirl momentum to axial flux of axial momentum, is generally used to describe the operating conditions of a co-annular swirling jet. According to Giannadakis, Perrakis, and Panidis[21] and Ivanic, Foucault, and Pecheux[22], it is given by:

$$S = \frac{\int_0^\infty U_y U_\theta \, r^2 dr}{R_O \int_0^\infty U_y^2 r \, dr}, \tag{5}$$

where U_y is the axial velocity, U_θ is the tangential velocity and R_O is the outer radius of the co-flow tube (see Fig. 2). Correlations for geometrical swirl numbers depend on the type of air swirler. Details about the correlations for geometrical swirl numbers can be found in Giannadakis, Perrakis, and Panidis[21]. According to Hardalupas and Whitelaw[12], based on the type of the air swirler used in this project, the geometrical swirl number is given by:

$$S = \frac{2}{3} \tan\theta \, \frac{1 - \left(\frac{D_O}{D_G}\right)^3}{1 - \left(\frac{D_O}{D_G}\right)^2}, \tag{6}$$

TABLE II. Operating conditions for the atomizer. B: bag breakup regime; F: fiber-type atomization; BF: boundary of fiber-type atomization (reproduced from Liang, Johansen, and Linne[2], with the permission of AIP Publishing).

Case	$\dot{m}_g$ (kg/h)	We_A	M	S	Breakup regime	U_l (m/s)	Re_l
1	16	256	384	0	B	0.11	438
2	18	324	486				
3	16	1126	1689	0.3			
4	18	1426	2139				
5	16	1126	1689	0.8	B		
6	18	1426	2139		BF		
7	16	1126	1689	1.2	B		
8	18	1426	2139		BF		
9	8	282	423	1.5	F		
10	10	440	660				
11	8	282	423	2.5			
12	10	440	660				
13	8	282	423	3.1			
14	10	440	660				
15	8	282	423	3.9			
16	10	440	660				

where θ is the swirl vane angle, D_0 is the external diameter of the liquid tube, and D_G is the diameter of the vane pack hub.

The operating conditions of the atomizer are shown in Table II. The conditions presented there are a subset of the larger set of conditions reported by Liang, Johansen, and Linne[2]. Lasheras and Hopfinger[13] pointed out that at large We_A (greater than 316), the breakup of a coaxial non-swirling air jet occurs in the forms of fibers, which produces finer droplets. This is called fiber-type atomizaion. As mentioned in Sec. I, the aim of this paper is to investigate how S and We_A influence the breakup of a central laminar liquid jet within the fiber-type atomization regime. Here, the magnitudes of We_A were chosen based on the rule that the operating conditions under each swirl number should be within that atomization regime. However, in this work, there is an experimental limit to the maximum of We_A that can be reached. Hence, for a few flow cases with $S \leq 1.2$, the operating conditions are within the bag breakup regime. The critical swirl number for our nozzle is equal to 0.8 (following Hopfinger and Lasheras[10]).

C. Experimental Procedure

For high-speed shadowgraphy, a Phantom VEO 710L high-speed camera acquired images of the jets. The spatial resolution was 119 μm/pixel and the exposure time was 30 μs. This spatial resolution was based on the fact that locating the camera closer to the jet to achieve better resolution would have flooded it with water. The selected exposure time was much smaller than the time scales in the coaxial air flows, which ensures that each individual shaodowgram is an instantaneous image.

A liquid jet turn-off behaviour was observed when S increased to 2.5 (this behaviour is described in more detail in Sec. III B). In order to study the underlying mechanisms behind the turn-off behaviours, POD was performed on the high-speed images (the approach to POD is described in detail in Liang, Johansen, and Linne[2]).

A phase Doppler particle analyzer (Artium Inc) was used to measure the size and velocity distributions of the droplets produced by the atomizer. The measurable droplet size and velocity ranges were from 1 μm to 195 μm, and from -133 m/s to 368 m/s, respectively. The sprays were measured at two downstream positions of $5D_l$ and $10D_l$, and at five radial positions of $-7.5D_l$, $-5D_l$, $-2.5D_l$, 0, $2.5D_l$, $5D_l$ and $7.5D_l$. Those measurement positions were chosen based on the rule that the PDI probes should be placed in a region between the dense zone and periphery of the spray. For each flow case, 5000 samples were collected at each measurement point. A 2-D translation stage was not available owing to experimental limitations. Therefore, the horizontal and vertical nozzle support beams were marked using a camera calibration, and the nozzle was moved by hand to change the positions of the measurement probes relative to the nozzle. The uncertainty of moving the nozzle by hand was evaluated and found to be between 0.5 mm and 1 mm ($\sim 5\% - 10\%$ of the radial interval between two measuring points).

As mentioned in Sec. I, we utilised SPIV to investigate the annular air flow fields in the companion paper[2]. Since droplet size and velocity distributions were related to the annular air flow fields (this is discussed in more detail in Sec. III A), the SPIV set-up will be briefly introduced here. 3.5 μm graphite particles were used as the seed material, with a Stokes number much less than 1. A 10 Hz dual-pulse Nd: YAG laser (Quantel Inc.) at a wavelength of 532 nm was used to illuminate the seed particles. Two Phantom VEO 710L cameras with Scheimpflug mounts acquired images of the swirling and non-swirling air jets. The laser sheet thickness at the jet centerline was 2.1 mm, as measured by a WinCamD (DataRay Inc). The laser sheet was aligned with the center of the nozzle exit. A programming timing unit (PTU, Lavision Inc) was used to synchronize the laser and the two cameras. The double-frame raw images were processed using Davis 10.2 to calculate 2D vector fields for each camera. More detail about the SPIV set-up can be found in Liang, Johansen, and Linne[2].

III. RESULTS AND DISCUSSION

A. Droplet Size and Velocity Distributions

The breakup of coaxial air-water jets involves the interaction between the gas and liquid phases. Hence, the annular air flow fields can influence droplet size and velocity distributions. The annular air flow fields and vorticity maps, which were obtained via SPIV, are presented here (see Fig. 3 and Fig. 4). Significantly more detail, including turbulence statistics, can be found at the online database[3]. Liang, Johansen, and Linne[2] found that a central reversal air flow occurs when $S \geq 1.2$ (see Fig. 3). Recirculating air flows affect the droplet velocity distributions (this is discussed in more detail in the rest of this subsection). In the companion paper, it was reported that radial expansion of the annular swirling air jets was observed near the nozzle exit, and it becomes larger as S goes up. When S remains constant, the extent of the radial expansion of the annular swirling air flows does not change as We_A is varied. Note that SPIV measurements were done for the annular air flows with medium We_A (≤ 440). We did not do SPIV for part of the flow cases with $440 < We_A \leq 1426$ in this paper, owing to a particle density problem, although there is no dependence of the radial expansion on We_A. When We_A increases, the topologies of the air flow fields do not change, except for the magnitudes of the velocity vectors. The value of S determines the extent of the radial expansion of the annular swirling air flows. Note that we discuss the annular air flows with specific We_A, despite the fact that the liquid was not flowing when we did SPIV measurements. By this we mean to designate the air flows used to create a specific We_A. Since, when flowing, the liquid jet flow rate was not changed, it is the air flow rate that sets We_A.

Figure 4 shows how the outer and inner shear layers evolve when S varies, based on a vorticity map. Note that the definition of a shear layer is the layer where the velocity gradient starts[2]. It was found that the inner and outer shear layers shifted towards the nozzle exit when S increased (see Figure 4). There is no dependence of shear layer evolution on We_A. This can be explained by the fact that S determines the extent of the radial expansion of the annular swirling air flows, as mentioned above. In this paper, we found that recirculating air flows and vortices, which were proved in the companion paper[2], influence droplet size and velocity distributions, as discussed in more detail in the rest of this subsection.

Figure 5 shows the radial distributions of the median droplet diameters (D) for various swirl numbers at two downstream positions of $5D_l$ and $10D_l$. Note that the median droplet diameter is presented here instead of the Sauter mean diameter (D_{32}).

As mentioned in Sec. II C, for each operating condition, 5000 droplet samples were collected at each measurement position. At a certain measurement position, if the diameter of a droplet is more than 1.5 times the interquartile range, away from the 25th or 75th percentiles of the droplet size data, they will be considered "outliers". For each droplet size dataset, the ratio of the number of "outliers" to the overall number of samples falls within the range of $\sim 0.9\% - 8.3\%$. Although those ratios are fairly low, it was found that at specific symmetrical measurement positions, if there is a very large "outlier" existing at either of those measurement positions, it will cause a significant difference in the value of D_{32} there. D_{32} tends towards the tail of positively skewed droplet distributions because the numerator of D_{32} contains the sum of the droplet diameters to the power of three. In effect, large droplets have a greater weight in the calculation of D_{32}. D_{32} can vary widely if there are significant outliers, when compared to the more robust median statistic. The median is insensitive to outliers while still including them in the calculation. Therefore, the median droplet diameter is presented here.

For each operating condition, the radial distribution of droplet diameters is symmetric with respect to the central axis of the nozzle exit. The droplet diameter distributions for all the operating conditions can be found in Liang, Johansen, and Linne[4], and the raw PDI data are included. For $S = 0$, droplets were detected from $r = -2.5D_l$ to $r = 2.5D_l$ at the downstream position of $5D_l$. As S increases to 0.3, the radial range within which the droplets distribute themselves expands to $[-5D_l, 5D_l]$ at that downstream position (see Fig. 5a and Fig. 5b). With further increase in S, droplets start to appear at the radial positions of $r = \pm 7.5D_l$, as expected (see Fig. 5a and Fig. 5b). This can be explained by the fact that as S increases, the droplets start to spread along the radial direction due to the radial expansion of the annular swirling air flows, as shown in Figure 3. Note that with the addition of air swirl, the radial ranges within which the droplets distribute themselves expand to $[-7.5D_l, 7.5D_l]$ at $y = 10D_l$ (see Fig. 5c and Fig. 5d).

D reduces somewhat as We_A increases, as expected, since the magnitudes of the aerodynamic forces acting on the liquid jets and the droplets increase. For $S = 0$ at $r = \pm 2.5D_l$, D increases somewhat further downstream (see Fig. 5). This can be caused by the collisions between droplets, which consequently leads to droplet coalescence. Droplet coalescence was also observed by Lasheras, Villermaux, and Hopfinger[7] when they used high-speed shadowgraphy and PDI to investigate a coaxial non-swirling air-water jet. They found that secondary breakup and coalescence of the droplets in the far field of the spray jet mainly depend on the total kinetic energy flux (mainly contained in the air jet) per unit total mass of the spray jet. Their total kinetic energy per unit time per unit total mass of air and water ranges from 23 $\mathrm{kJ/(kg \cdot s)}$ to 1.9×10^6 $\mathrm{kJ/(kg \cdot s)}$, and in this work, it ranges from 9.5×10^3 $\mathrm{kJ/(kg \cdot s)}$ to 1.4×10^4 $\mathrm{kJ/(kg \cdot s)}$ which is a subset of their kinetic energy range.

Dunand, Carreau, and Roger[14] ejected a turbulent water jet into a coaxial air jet with S and M in the ranges of $\sim 0 - 0.6$ and $\sim 3 - 13.3$, respectively. They found that when S goes beyond S_{cr}, small droplets are located in the hollow-cone region caused by the recirculating air flows, while large droplets appear on the jet periphery. They also found that the droplet size distributions with $S < S_{cr}$ are opposite to the ones with $S > S_{cr}$. However, in this work, D tends to be unrelated to S (see Fig. 5 and Fig. 6). This is because the spray morphologies for the breakup of the central laminar and turbulent liquid jets are different. Hollow-cone spray structures were not observed in this work due to the low kinetic energy contained in the central laminar liquid jet (this is discussed in more detail in Sec. III B). As mentioned in Sec. I, Hardalupas and Whitelaw[12] investigated the breakup of a central turbulent water jet by a co-annular air jet with S in the range of $\sim 0 - 7.9$. They utilised PDI to measure the diameters, velocities and liquid fluxes of the droplets over a small range of aerodynamic Weber numbers, $We_A(230 - 630)$. They found that for $S = 0$ with We_A in the range of $494 - 598$, the median droplet diameters at $Y = 26D_l$ ranged from 148 μm to 159 μm. Those median droplet diameters are much larger than the median droplet diameters generated by the coaxial non-swirling jet in this work (< 20 μm) (see Figs. 5a and 5b). This implies that turbulence in the liquid generates bigger drops. This point can be explained by the fact that droplet sizes partly depend on spray morphologies which are differ-

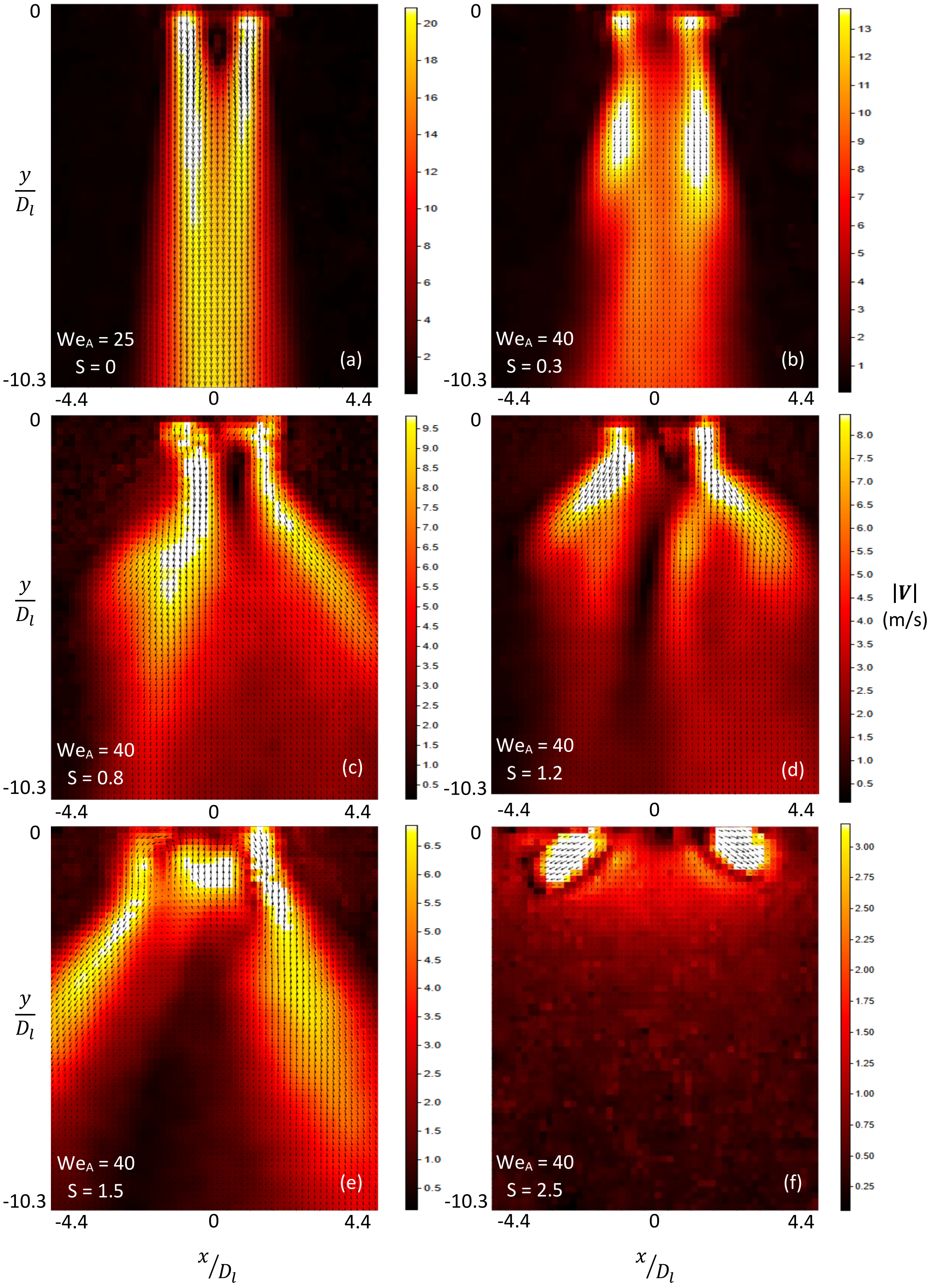

FIG. 3. 3D vector fields projected onto the 2D planes for various swirl numbers (reproduced from Liang, Johansen, and Linne[2], with the permission of AIP Publishing).

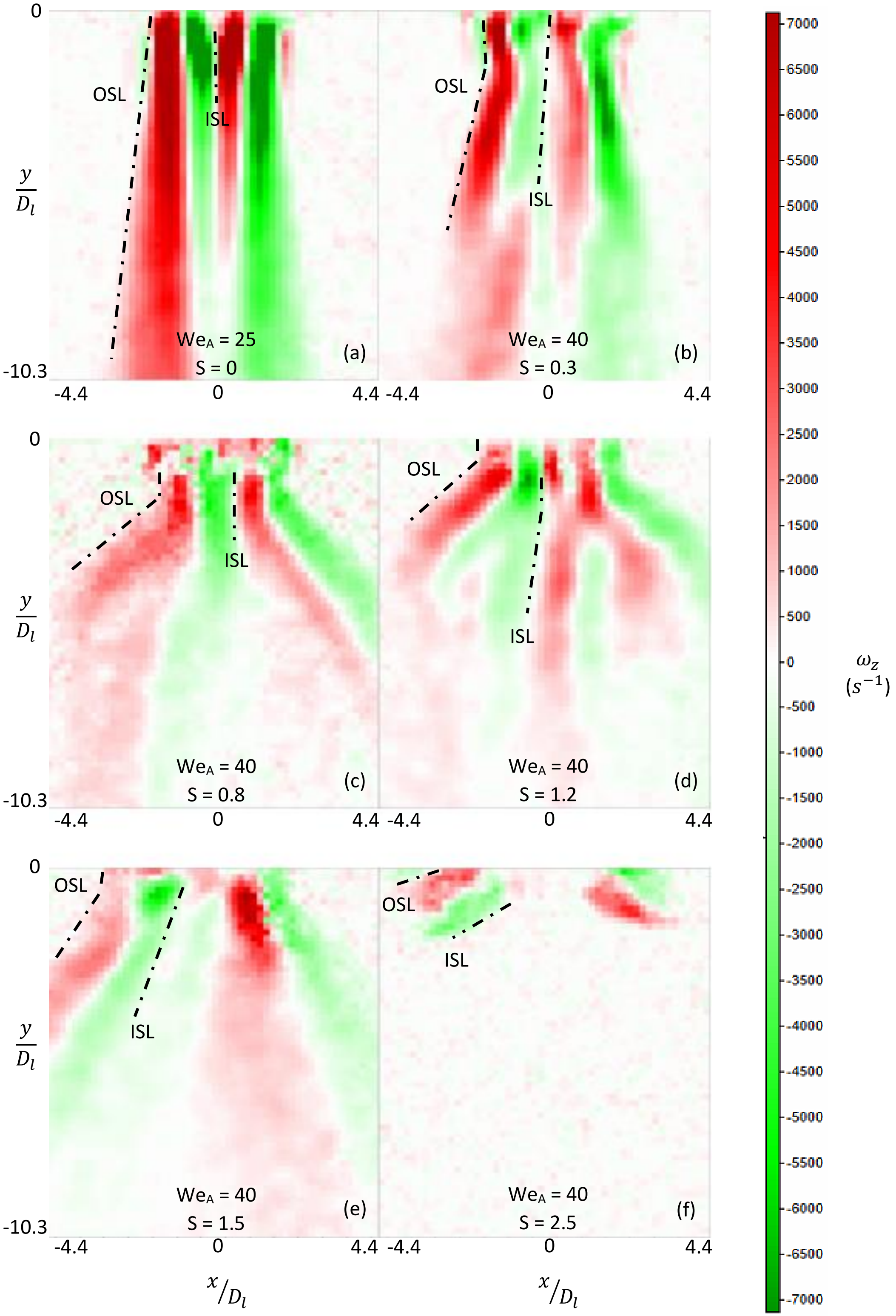

FIG. 4. Vorticity maps for various swirl numbers. OSL: outer shear layer; ISL: inner shear layer (reproduced from Liang, Johansen, and Linne[2], with the permission of AIP Publishing).

ent for the breakup of the central laminar and turbulent liquid jets. As one of the breakup mechanisms, turbulence in the liquid influences spray morphologies in a way that changes the jet velocity profile and makes a difference to the shear instability. The sizes of the droplets, which are peeled off from the liquid jet surface due to shear instability, are therefore influenced by the turbulence in the liquid. Lasheras, Villermaux, and Hopfinger[7] measured D_{32} at $r = 0$ at the axial range of $[10D_l, 133D_l]$ when they investigated a non-swirling air-water jet with Re_l ranging from 494 to 2086, and with We_A of the order of 1267. They found that D_{32} increases with Re_l at all measurement positions, which also indicates that turbulence in the liquid tends to generate bigger drops. Similarly, Eroglu and Chigier[9] ejected a water jet into coflowing air without swirl. They measured the radial distributions of D_{32} at $y = 10D_l$ for Re_l ranging from 1453 to 2519, and for We_A of the order of 277. They found that D_{32} increases as Re_l increases, which is consistent with what Lasheras, Villermaux, and Hopfinger[7] found.

Figure 7 shows the relationship between the swirl numbers and the axial velocities of the droplets at the downstream position of $5D_l$. The coordinate system is shown in figure 2. The statistical distributions of the axial velocities of the droplets are shown using box plots (see Fig. 7). Note that the central line of each box indicates the median. The top and bottom edges of each box represent 25th and 75th percentiles, respectively. Whiskers extend to the most extreme points. If sample values are more than 1.5 times the interquartile range away from the bottom or top edges of the boxes, they will be considered "outliers" and will be plotted using circular symbols. It was found that when $S \geq 0.8$, some of the droplets ($< 25\%$) located at the central axis of the nozzle start to move upward. This can be explained on the basis of recirculating air flows, as shown in Figure 3 and discussed by Liang, Johansen, and Linne[2]. For $S = 0.3$ and $S = 0.8$, the differences between the medians of the axial velocities at $r = \pm 2.5$ are of the order of 53%. It can be found that for $S = 0.3$ and $S = 0.8$, 75% of the statistical distributions at $r = \pm 2.5D_l$ overlap with each other (see Fig. 7). Note that recirculating air flows occur for $S = 0.3$ and $S = 0.8$ which are indicated by the positive axial velocities of droplets (see Fig. 7). Although 75% of the statistical distributions at $r = \pm 2.5D_l$ overlap with each other, recirculating air flows and vortices (as indicated in Fig. 4) can cause variation in the median of the axial velocities. When S increases from 0.3 to 0.8, the radial location where the droplets with higher velocities were detected changes from $r = 2.5D_l$ to $r = -2.5D_l$. This can be explained on the basis of the recirculating air flows which are indicated by upward motion of droplets for $S = 0.3$ and $S = 0.8$ (see Fig. 7). Note that Figures 3 and 4 are the average 3D vector fields and vorticity maps, respectively. The average results were presented since the frequency of the dual-pulse Nd: YAG laser was low (10 Hz). However, when we observed instantaneous air flow fields using a high-speed laser, we observed vortices and central recirculating air flows which were unsteady. The intensities and streamlines of recirculating air flows and vortices vary with time. When S increases from 0.3 to 0.8, switching of the high velocity point from $r = 2.5D_l$ to $r = -2.5D_l$ can be explained on the basis of the unsteadiness of recirculating air flows and vortices. It was found that when $S \geq 0.3$, upward motion of droplets located at the central axis of the nozzle was observed at the downstream position of $10D_l$. For each measurement position, the axial velocity of the droplet increases as We_A increases, as expected. This can be explained by the fact that when shear forces increase, liquid lumps pinch off from the liquid core with higher velocities. Momentum transfer between the liquid lumps and surrounding high-speed air occurs[7]. This causes the acceleration of liquid lumps, together with breakup and coalescence of drops (Lasheras, Villermaux, and Hopfinger[7]). The breakup of those liquid lumps can lead to droplets with high velocities.

Figure 8 shows the relationship between the swirl numbers and the radial velocities of the droplets at the downstream position of $5D_l$. It was found that for S in the range of $\sim 0 - 0.8$, most of the droplets ($\geq 75\%$) located at $r = \pm 2.5D_l$ are blown outward away from the central axis of the nozzle at the downstream position of $5D_l$. However, when S increases to 1.5, 75% of the droplets located at $r = 2.5D_l$ are blown inward to the central axis of the jet. As S increases to 2.5, 50% of the droplets located at $r = \pm 2.5D_l$ move inward (see Fig. 8). This can be explained by the fact that when high swirl ($S \geq 1.2$) is added into the annular air jet, a strong central recirculating air flow occurs (see Fig. 3). As a result, the reversal air flows change the statistical distributions of the radial velocities of the droplets.

B. Turn-off behaviour

The high-speed shadowgrams indicate that when S increases to 2.5, recirculating air flows start to penetrate to the water tube, which momentarily stops portions of the central laminar water jets from exiting, called the turn-off behaviour here. Those central recirculating air flows were observed in the SPIV measurements (see Fig. 3f). Figure 9b illustrates the turn-off behaviour for flow case 15 ($S = 3.9$, $We_A = 282$). Note that Figures 9a and 9b were produced by applying background subtraction to the high-speed shadowgrams. In order to study the turn-off behaviour qualitatively and quantitatively, spatial POD was performed on the high-speed images for all the swirling flow cases mentioned in Table II. The spatial POD can be determined using singular value decomposition (SVD)[2,23]. How spatial POD was applied to the jet shadowgrams was presented in the companion paper[2]. Therefore the algorithm for spatial POD is only introduced here. A rectangular matrix can be decomposed with SVD[23]. According to Strang[24], after decomposed with SVD, a n by m matrix

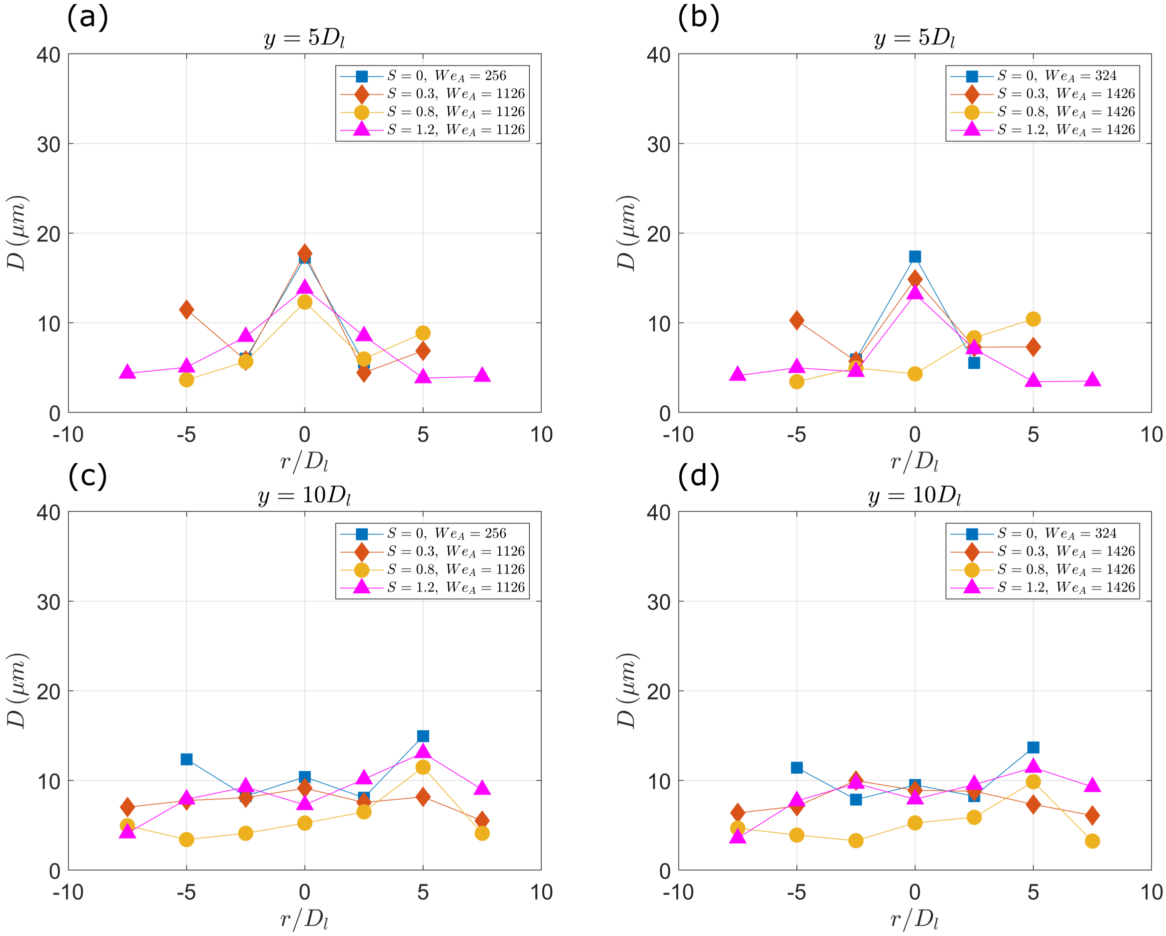

FIG. 5. Distributions of median droplet diameters (D) for $S = 0 - 1.2$ at $y = 5D_l$ and $y = 10D_l$. (a) Distributions of D for cases 1, 3, 5 and 7 at $y = 5D_l$. (b) Distributions of D for cases 2, 4, 6 and 8 at $y = 5D_l$. (c) Distributions of D for cases 1, 3, 5 and 7 at $y = 10D_l$. (d) Distributions of D for cases 2, 4, 6 and 8 at $y = 10D_l$.

$\boldsymbol{K}$ is given by:

$$\begin{aligned}\boldsymbol{K} = \boldsymbol{U}\boldsymbol{\Sigma}\boldsymbol{V}^T &= [\boldsymbol{u}_1, \boldsymbol{u}_2, \ldots, \boldsymbol{u}_r] \begin{bmatrix} \sigma_1 & 0 & \ldots & 0 \\ 0 & \sigma_2 & \ldots & 0 \\ \vdots & \vdots & \ddots & \vdots \\ 0 & 0 & 0 & \sigma_r \end{bmatrix} \begin{bmatrix} \boldsymbol{v}_1^T \\ \boldsymbol{v}_2^T \\ \vdots \\ \boldsymbol{v}_r^T \end{bmatrix} \\ &= \boldsymbol{u}_1\boldsymbol{\sigma}_1\boldsymbol{v}_1^T + \boldsymbol{u}_2\boldsymbol{\sigma}_2\boldsymbol{v}_2^T + \ldots + \boldsymbol{u}_r\boldsymbol{\sigma}_r\boldsymbol{v}_r^T, \qquad (7) \\ \boldsymbol{K} \in \mathbb{R}^{n\times m}, &\boldsymbol{U} \in \mathbb{R}^{n\times r}, \boldsymbol{V} \in \mathbb{R}^{m\times r}, \boldsymbol{\Sigma} \in \mathbb{R}^{r\times r}, \\ &\sigma_1 \geq \sigma_2 \geq \ldots \geq \sigma_r > 0,\end{aligned}$$

where, r is the rank of the matrix $\boldsymbol{K}$, $\sigma_i, i = 1, 2, ..., r$, denote singular values, the superscript T denotes transpose, and $\boldsymbol{u}_i, \boldsymbol{v}_i, i = 1, 2, ..., r$ are called left singular vectors and right singular vectors, respectively[24]. $\boldsymbol{u}_i, i = 1, 2, ..., r$, are also called the POD modes[23]. For visualisation of the POD modes, the left singular vector $\boldsymbol{u}_i$ can be rearranged into a matrix with the same dimension as the shadowgrams. Since the matrix $\boldsymbol{V}$ contains the temporal components of matrix $\boldsymbol{K}$, performing a Fourier transform on matrix $\boldsymbol{V}$ generates the frequency of each mode[2]. Generally, the singular value distribution of a POD mode is used to evaluate how important that POD mode is among all the principal components. According to Liang, Johansen, and Linne[2], the singular value distribution (ε_i) of a POD mode is given by:

$$\varepsilon_i = \frac{\lambda_i}{\sum_{j=1}^{j=r} \lambda_j}, i \geq 1, \qquad (8)$$

where λ_i is the singular value for that POD mode, and r is total number of non-zero singular values and the rank of $\boldsymbol{K}$ in Eq. 7.

It was found that the turn-off behaviours appear as the first modes for cases 12 and 15 (see Fig. 10 and Fig. 11). This is consistent with what we observed using high-speed shadowgraphy. Note that for each figure, the values are normalized by their respective maxima. The positive and negative magnitudes reveal the spatial patterns which occur at different moments. Figures 10 and 11 show that for each first POD mode, there is a central region with large positive values (> 0.5), which accounts for the turn-on condition, while there are small regions with small negative values (< -0.5) near the nozzle exit, which accounts for the turn-off condition. Note that the turn-off condition is caused by recirculating air flows

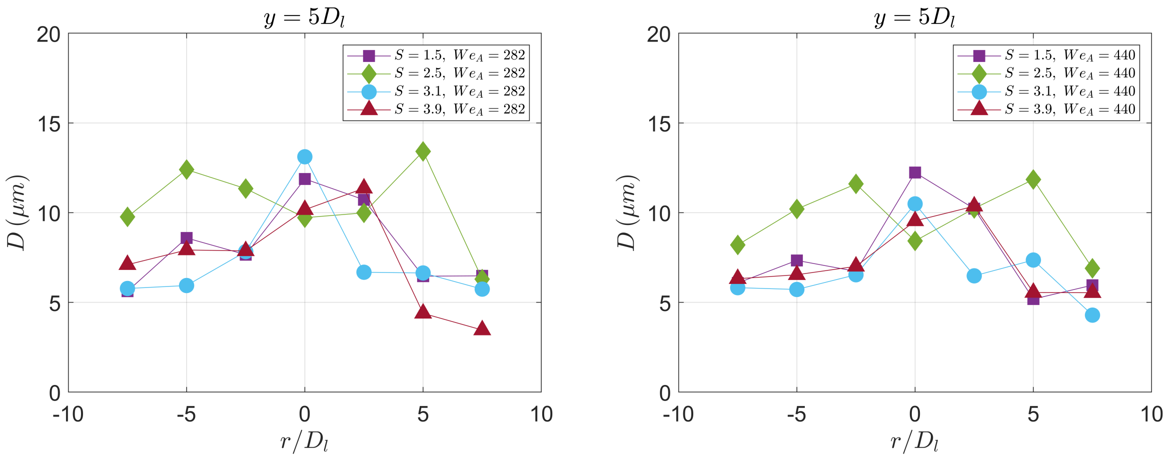

FIG. 6. Distributions of median droplet diameters (D) for $S = 1.5 - 3.9$ at $y = 5D_l$.

which stop portions of the central laminar water jets from exiting, rather than stopping all of the water jets (see Fig. 9). This is why there are small blue regions near the nozzle exit in the first POD mode, which represents a few of the water jets exiting from the water tube when the turn-off behaviour occurs. In figures 10 and 11, the interpretation on the topology of each POD mode is consistent with what was observed using high-speed shadowgraphy. The first POD mode was used to reconstruct the shadowgrams, and it was found that the turn-on and turn-off conditions occur in the reconstructed images. This confirms that the first POD mode accounts for the turn-on and turn-off conditions. The reconstructed images using the first four POD modes, and the high-speed videos for all the flow cases can be found in the online database[4]. Note that ε_1' is much larger than ε_1, which implies that the turn-off behaviour (as revealed by the first POD mode) becomes more dominant when S increases from 2.5 to 3.9 (see Fig. 10 and Fig. 11).

In order to study the turn-off behaviour quantitatively, a fast Fourier transform was performed on the first column of matrix $\boldsymbol{V}$ to yield the frequency of the turn-off behaviour which is revealed by the first POD mode (see Eq. 7). A broad spread of frequencies of almost equal amplitude was observed in the frequency spectra of the first POD modes for those two flow cases. This means that the timing of turn-off initiation is random for cases 12 and 15. However, it was found from the high-speed shadowgraphy measurements that for case 12, each turn-off event exists for around 7.5×10^{-4} s, while for case 15, it exists for a period of time between 3.33 ms and 6.67 ms. This is as expected, since as S increases, a wide range of recirculating air flows occur (see fig. 3), and as a result they stop portions of the central laminar water jets from exiting for a longer time. Note that the durations of each turn-off event are consistently the times given here. This observation is in contrast to the timing of turn-off initiation, which tends to be random. The liquid mass flow controller could potentially have an effect on the turn-off behaviours because it is designed to maintain flow, but if it does we expect the effect to be small. The duration of each turn-off event is much shorter than the update time of the liquid mass flow controller (50 ms). The controller would not respond fast enough to overpower the turn-off events. If anything, the turn-off behaviours may have a small effect on the average liquid flow rate. The high-speed videos for all the flow cases mentioned in Table II can be found in Liang, Johansen, and Linne[4].

Turn-off behaviour has not been reported by other researchers mentioned in Sec. I, since their central liquid jets were turbulent. They observed hollow-cone spray structures instead, which was not observed in this work. An equilibrium among the static pressure, the kinetic energy of the liquid jet and gas flow, and the ambient pressure should be achieved to sustain the hollow-cone spray structure[2,10]. However, in the present study, the kinetic energy inside the central laminar water jet is not high enough to fulfil that requirement, and as a result for the high swirling flow cases ($S \geq 2.5$), the upward air flows with high momentum tend to momentarily stop portions of the central laminar water jets from exiting instead.

IV. CONCLUSIONS

The goal of the work reported here, together with that of Liang, Johansen, and Linne[2], is to develop a comprehensive database for spray formation caused by shear forces, in part by removing turbulence from the liquid jet. In order to investigate how the strength of the air swirl influences spray formation, air swirl is introduced into the annular air flows using four-vane swirlers with S in the range of $0.3 - 3.9$. PDI was utilised to measure the droplet size and velocity distributions. High-speed shadowgraphy was utilised to visualise the spray behaviour, and the turn-off behaviours were observed for the high swirling flow cases ($S \geq 2.5$). POD was performed on the shadowgrams to study the underlying mechanisms behind the turn-off behaviour. The droplet size and velocity distributions, results of the POD analysis, and high-speed videos for all the flow cases, are stored in the online database[4]. The following statements are concluded from the measurements.

1. As S increases, the atomization of a central laminar wa-

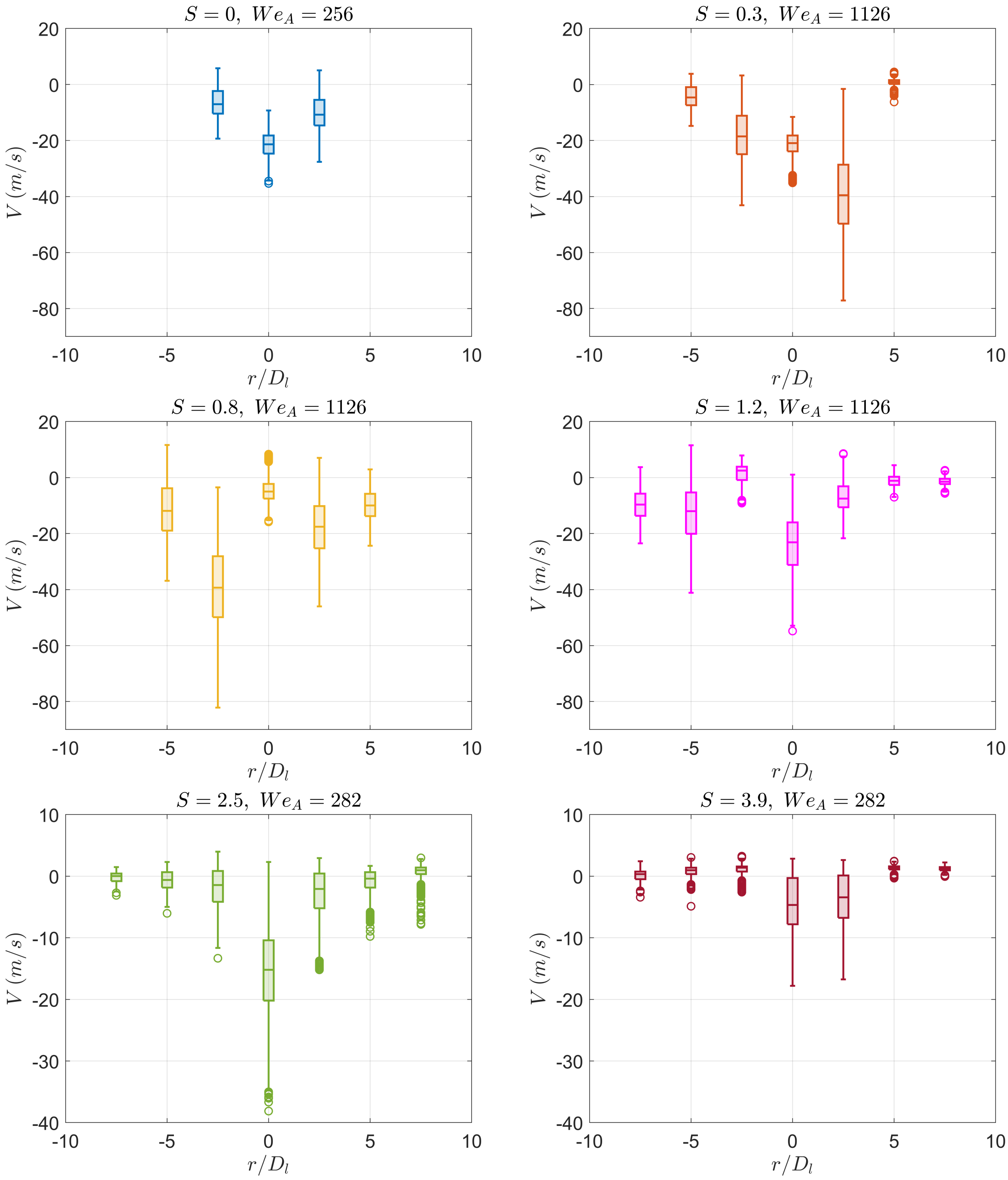

FIG. 7. Axial velocity distributions of droplets for $S = 0 - 3.9$ at $y = 5D_l$.

ter jet is improved in a way that the droplets are blown outward from the central axis of the nozzle, which is consistent with what Hardalupas and Whitelaw [12] found when they investigated the breakup of a turbulent jet by a coaxial swirling air stream. However, in the present study, for the coaxial jets within bag breakup regimes with $Re_l = 438$ and S in the range of $\sim 0 - 0.3$, D was found to be not related to S. For the coaxial jets within fiber-type atomizaton regime or on the boundary of fiber-type atomization regime with $Re_l = 438$ and S in the range of $\sim 0.8 - 3.9$, D was found to be not related to S. For $S \geq 0.3$, upward motion of droplets located at the central axis of the nozzle was observed, which was caused by recirculating air flows.

2. When S increases to 2.5, recirculating air flows start to penetrate to the water tube, which momentarily stops portions of the central laminar water jets from exiting. This is called the turn-off behaviour. The timing of turn-off initiation is random.

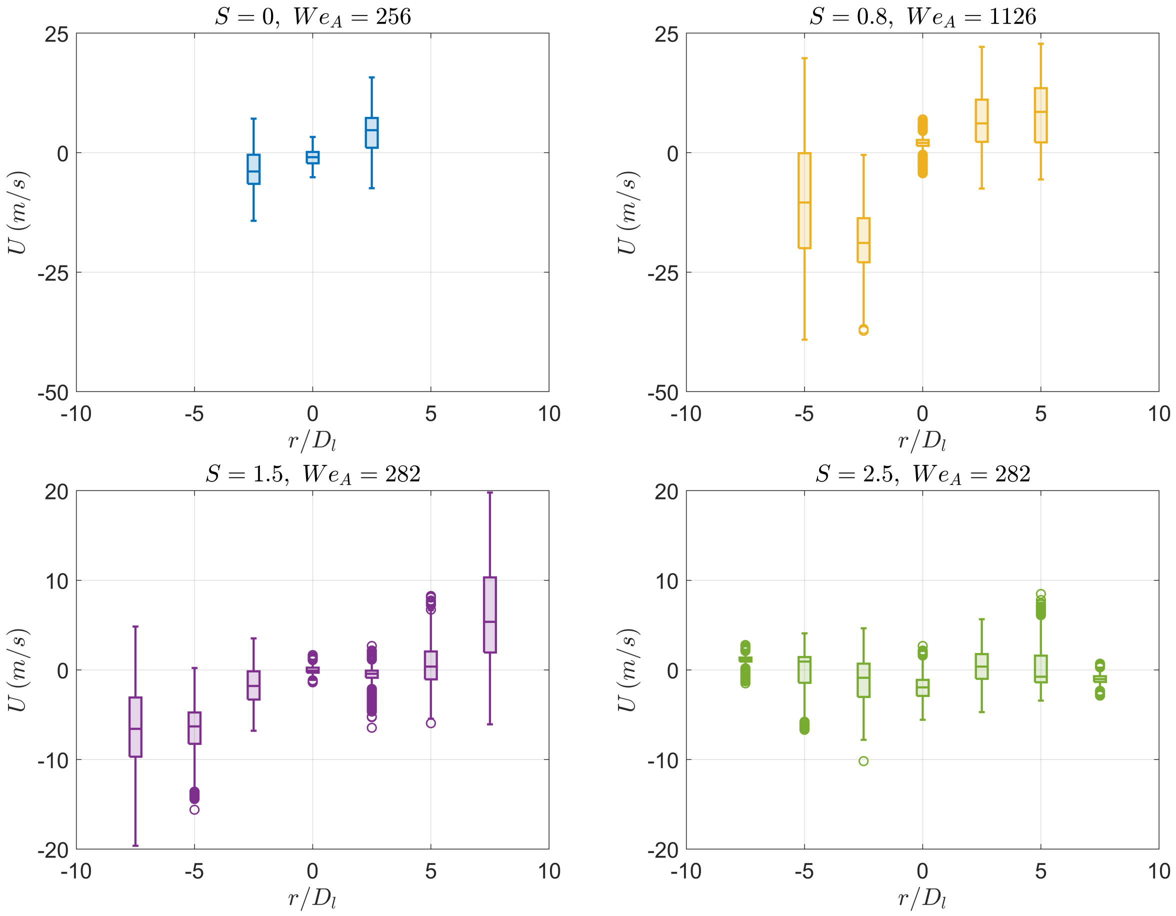

FIG. 8. Radial velocity distributions of droplets for $S = 0,\ 0.8,\ 2.5$ and 3.9 at $y = 5D_l$.

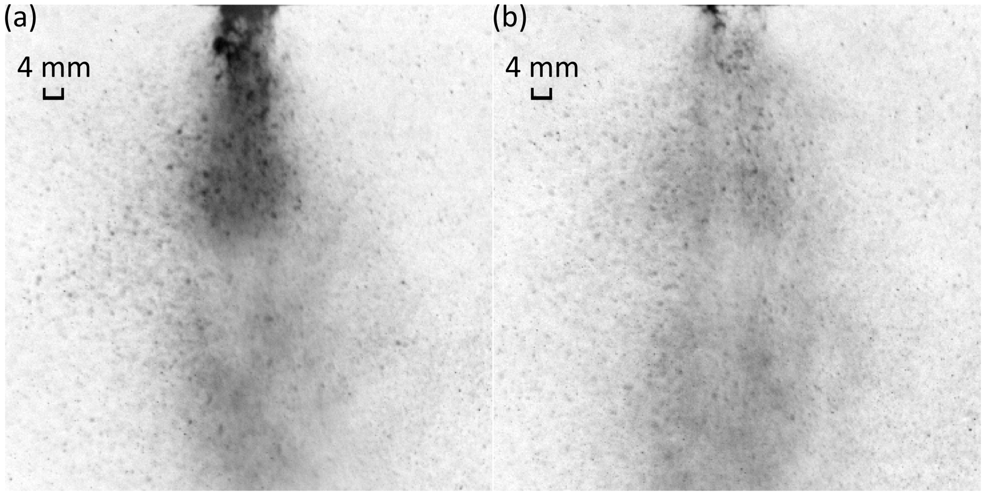

FIG. 9. Shadowgrams that reveals the turn-off behaviour ($S = 3.9$, $We_A = 282$). (a) Turn-on condition. (b) Turn-off condition.

ACKNOWLEDGMENTS

This work was supported in part by EPSRC grants number EP/P020593/1 and EP/P011438/1.

DATA AVAILABILITY STATEMENT

The data that support the findings of this study are openly available in Edinburgh DataShare at https://doi.org/10.7488/ds/3478[4].

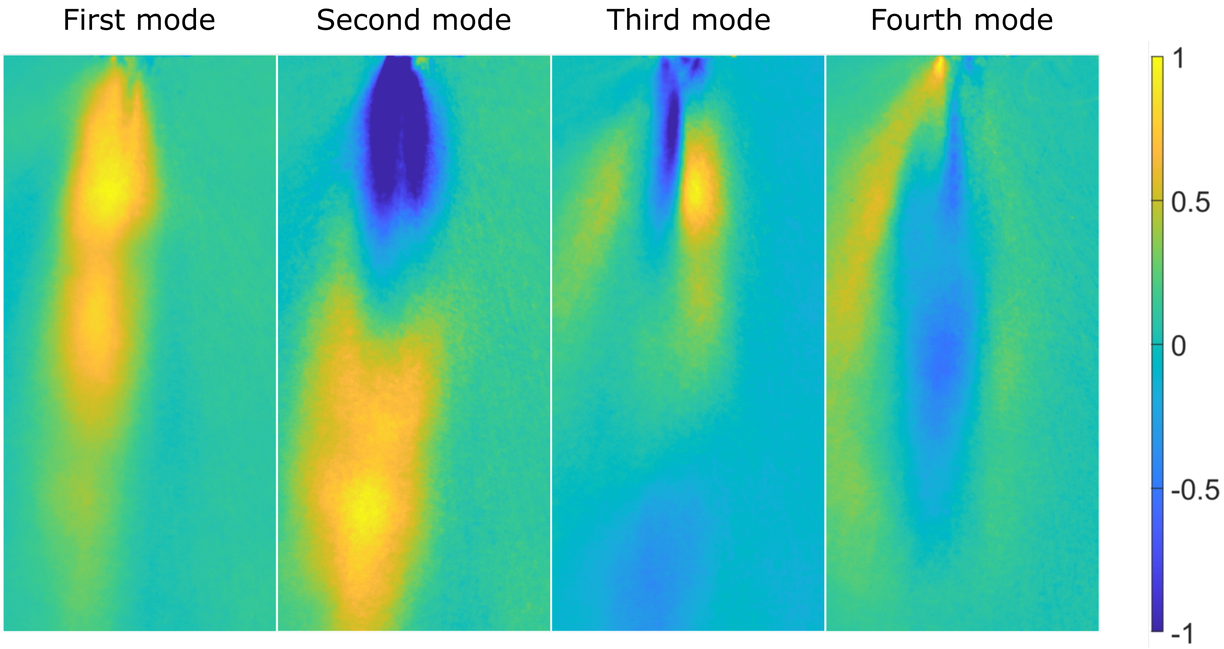

FIG. 10. First four POD modes for case 12 ($S = 2.5$, $We_A = 440$). The singular value distributions of the first (ε_1), second (ε_2) and third (ε_3) modes are 0.0063, 0.0047, 0.0031 and 0.0026, respectively.

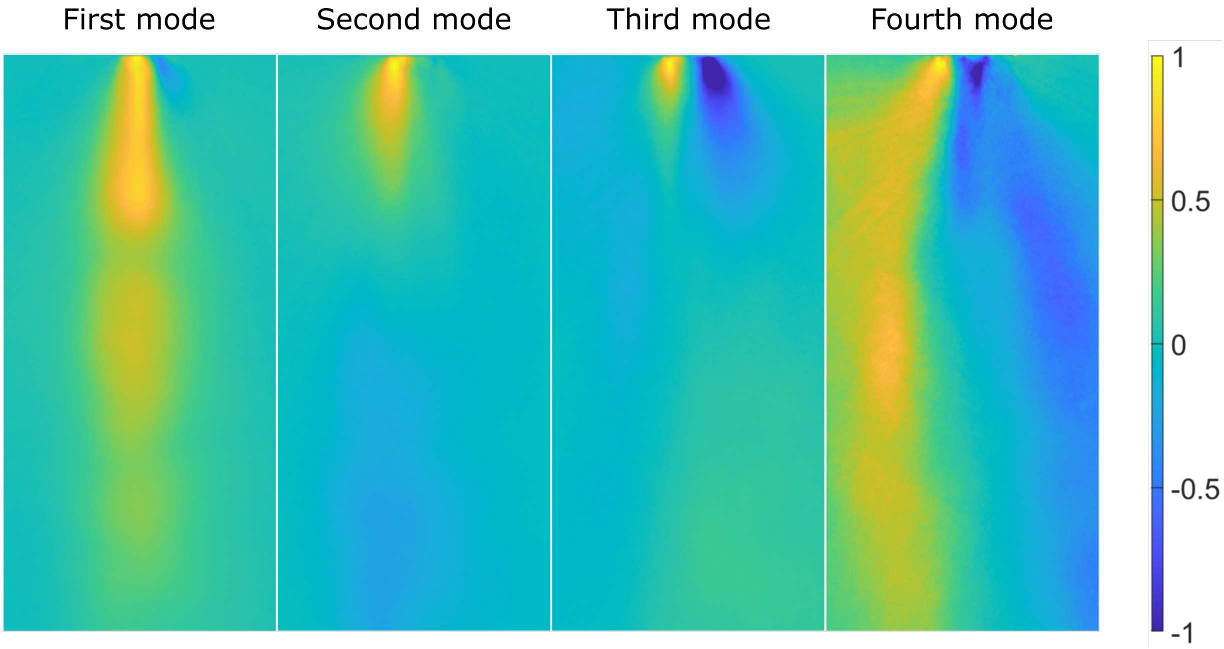

FIG. 11. First four POD modes for case 15 ($S = 3.9$, $We_A = 282$). The singular value distributions of the first (ε_1'), second (ε_2') and third (ε_3') modes are 0.0166, 0.009, 0.0082 and 0.0065, respectively.

REFERENCES

[1] A. H. Lefebvre and V. McDonell, *Atomization and Sprays (2nd Edition)* (CRC Press, 2017).

[2] Y. Liang, L. C. Johansen, and M. Linne, "Breakup of a laminar liquid jet by coaxial non-swirling and swirling air streams." Physics of Fluids (2022), (in press). Https://doi.org/10.1063/5.0100456.

[3] Y. Liang, L. C. Johansen, and M. Linne, "Breakup of a laminar liquid jet by coaxial non-swirling and swirling air streams," University of Edinburgh (2022), dataset. https://doi.org/10.7488/ds/3459.

[4] Y. Liang, L. C. Johansen, and M. Linne, "Characteristics of sprays produced by coaxial non-swirling and swirling air-water jets with high aerodynamic Weber numbers," University of Edinburgh (2022), dataset. Https://doi.org/10.7488/ds/3478.

[5] C. M. Varga, J. C. Lasheras, and E. J. Hopfinger, "Initial breakup of a small-diameter liquid jet by a high-speed gas stream," J. Fluid. Mech **497**,

405–434 (2003).

[6] L. Yang, Y. Gao., J. Li, and Q. Fu, "Theoretical atomization model of a coaxial gas-liquid jet," Physics of Fluids **32** (2020).

[7] J. C. Lasheras, E. Villermaux, and E. J. Hopfinger, "Break-up and atomization of a round water jet by a high-speed annular air jet," J. Fluid Mech **357**, 351–379 (1998).

[8] Y. Hardalupas and J. H. Whitelaw, "Characteristics of sprays produced by coaxial airblast atomizers," Journal of Propulsion and Power **10**, 453–460 (1994).

[9] H. Eroglu and N. Chigier, "Initial drop size and velocity distributions for airblast coaxial atomizers," Journal of Fluids Engineering **113**, 453–459 (1991).

[10] E. J. Hopfinger and J. C. Lasheras, "Explosive breakup of a liquid jet by a swirling coaxial gas jet," Physics of Fluids **8**, 1696–1698 (1996).

[11] N. Machicoane, J. K. Bothell, D. Li, T. B. Morgan, T. J. Heindel, A. L. Kastengren, and A. Aliseda, "Synchrotron radiography characterization of the liquid core dynamics in a canonical two-fluid coaxial atomizer," International Journal of Multiphase Flow **115**, 1–8 (2019).

[12] Y. Hardalupas and J. H. Whitelaw, "Coaxial airblast atomizers with swirling air stream," Recent advances in spray combustion: measurements and model simulation. **2**, 201–232 (1998).

[13] J. C. Lasheras and E. J. Hopfinger, "Liquid jet instability and atomization in a coaxial gas stream," Annual Review of Fluid Mechanics **32**, 275–308 (2000).

[14] A. Dunand, J. L. Carreau, and F. Roger, "Liquid jet breakup and atomization by annular swirling gas jet," Atomization and Sprays **15**, 223–247 (2005).

[15] Z. W. Lian and S. P. Lin, "Breakup of a liquid jet in a swirling gas," Physics of Fluids **2**, 2134–2139 (1990).

[16] Y. Liao, S. M. Jeng, M. A. Jog, and M. A. Benjamin, "The effect of air swirl profile on the instability of a viscous liquid jet," J. Fluid. Mech **424**, 1–20 (2000).

[17] A. A. Ibrahim and M. A. Jog, "Nonlinear breakup of a coaxial liquid jet in a swirling gas stream," Physics of Fluids **18** (2006).

[18] F. M. White, *Fluid Mechanics* (McGraw-Hill, 2016).

[19] H. Schlichting and K. Gersten, *Boundary Layer Theory* (Springer, 2017).

[20] F. M. White, *Viscous Fluid Flow*, 3rd ed. (McGraw-Hill, 2005).

[21] A. Giannadakis, K. Perrakis, and T. Panidis, "A swirling jet under the influence of a coxial flow," Experimental Thermal and Fluid Science **32**, 1548–1563 (2008).

[22] T. Ivanic, E. Foucault, and J. Pecheux, "Dynamics of swirling jet flows," Experiments in Fluids **35**, 317–324 (2003).

[23] K. Taira, S. L. Brunton, S. T. M. Dawson, C. W. Rowley, T. Colonius, B. J. McKeon, O. T. Schmidt, S. Gordeyev, V. Theofilis, and L. S. Ukeiley, "Modal analysis of fluid flows: An overview," American Institute of Aeronautics and Astronautics **55**, 4013–4041 (2017).

[24] G. Strang, *Linear Algebra and Learning from Data* (Wellesley-Cambridge press, 2019).